Quantum optimal control using phase-modulated driving fields

Jiazhao Tian,[1,2] Haibin Liu ●,[1,2,*] Yu Liu,[1] Pengcheng Yang,[1] Ralf Betzholz ●,[1]
Ressa S. Said,[3] Fedor Jelezko,[3] and Jianming Cai[1,2]

[1]*School of Physics, International Joint Laboratory on Quantum Sensing and Quantum Metrology,*
Huazhong University of Science and Technology, Wuhan 430074, People's Republic of China
[2]*State Key Laboratory of Precision Spectroscopy, East China Normal University, Shanghai 200062, China*
[3]*Institute for Quantum Optics and Center for Integrated Quantum Science and Technology, Ulm University, D-89081 Ulm, Germany*

Quantum optimal control represents a powerful technique to enhance the performance of quantum experiments by engineering the controllable parameters of the Hamiltonian. However, the computational overhead for the necessary optimization of these control parameters drastically increases as their number grows. We devise a variant of a gradient-free optimal-control method by introducing the idea of phase-modulated driving fields, which allows us to find optimal control fields efficiently. We numerically evaluate its performance and demonstrate the advantages over standard Fourier-basis methods in controlling an ensemble of two-level systems showing an inhomogeneous broadening. The control fields optimized with the phase-modulated method provide an increased robustness against such ensemble inhomogeneities as well as control-field fluctuations and environmental noise, with one order of magnitude less of average search time. Robustness enhancement of single quantum gates is also achieved by the phase-modulated method. Under environmental noise, an XY-8 sequence constituted by optimized gates prolongs the coherence time by 50% compared with standard rectangular pulses in our numerical simulations, showing the application potential of our phase-modulated method in improving the precision of signal detection in the field of quantum sensing.

I. INTRODUCTION

As the extension of optimal control theory in the quantum realm, quantum optimal control (QOC) seeks the design of control fields that drive a quantum system to achieve certain tasks, such as state preparation [1–3], wave-function control [4–6], noise suppression [7–9], or the implementation of quantum logic gates [10–18]. It covers a wide range of fields of physics, chemistry, biology, medicine, and their cross disciplines. For example, QOC has important applications in magnetic-resonance spectroscopy and imaging, quantum information processing, quantum simulation, and quantum sensing [19].

The most prevailing numerical methods used in QOC are gradient-based methods, including the gradient ascent pulse engineering (GRAPE) method [10,20–23] and the Krotov algorithm [24–27]. They are mathematically nontrivial and work in high-dimensional control spaces [28]. On the other hand, gradient-free methods, e.g., the chopped random-basis (CRAB) method and its variants [29–32], that transform a functional optimization into a multivariable function optimization, work in reduced control space, and therefore are relatively simple to use and yet produce a smooth control field. There are other methods, however, including direct methods, which discretize the optimal control problem and use nonlinear optimization solvers [33,34], and synthetic methods, e.g.,

the gradient optimization of analytic controls (GOAT) method and the gradient optimization using parametrization (GROUP) method [28,35]. Generally speaking, gradient-based methods are more involved but provide better local optimal results. They work well for problems with straightforward target functions and no constraint conditions [36]. By contrast, the gradient-free parametrization methods can handle problems with more diversified target functions more efficiently. They also allow for explicit restrictions by choosing a suitable search method and are favorable when the gradient information is hardly accessible. Furthermore, the variety of easily available optimization solvers makes parametrization methods simple and flexible to use. However, the determination of a sufficient number of parameters in parametrized optimizations is crucial. Ideally, the number of parameters has to be increased until a convergence of the results is met. In practice, the balance between the improvement of the results and the increasing computational overhead has to be carefully maintained. Therefore, methods with sound optimal control results, less required parameters, and thereby shorter optimization time are highly demanded.

In this paper, we focus on the constrained optimization problem of the coherent control of a qubit ensemble with inhomogeneous broadening. We propose that a phase-modulated (PM) function basis is eminently suitable to construct the control field, since it shows the merit of finding favorable results in low-dimensional parameter spaces. Constrained by the same maximal field strength and the same maximal search resources, highly improved results are reached using one order

*liuhb@hust.edu.cn

of magnitude less of search time than the standard Fourier basis (SFB) used in the CRAB algorithm implementations (see, e.g., [11,37]). A phase-introduced version of SFB, referred to as SFB-P2, is proposed for a fairer comparison with the PM method in view of the fact that both methods possess control fields in two directions in the interaction picture. SFB-P2 improves the results of SFB as the number of parameter increases, and gives comparable results with the three-parameter PM method using 20 parameters and a search time one order of magnitude longer. Also, offering the same amount of total results with different initial values, PM possesses a much higher proportion of global optimal results than SFB-P2 with 20 parameters, demonstrating a more stable capability to find the global optimal results with limited resources. These advantages can be attributed to the ability of PM to contain multiple frequency components in the control fields constructed using the PM basis with fewer parameters. In lower-dimensional parameter spaces (i.e., three parameters for PM and four parameters for SFB-P2), these advantages become more prominent as the spectra of the ensemble inhomogeneity spread wider. Also, they hold in the presence of variations in the control fields and environment-induced dephasing, as the area bounded by the 90% fidelity contour in the detuning and field-variation plane for PM is much larger than the one for SFB-P2 in both cases, with and without dephasing noise. As a supplement, we also optimize the average fidelity of single qubit gates with inhomogeneous broadening using the PM method, and apply it to the XY-8 pulse sequence, where the simulated coherence time is prolonged by 50% compared with the rectangular pulses of equal maximal pulse strength. Combined with the randomization method, PM can be categorically classified into the CRAB-method family as a capable tool for solving problems including single spin systems under ambient noise, spin ensembles, and many-body systems.

The structure of the paper is as follows. In Sec. II, we describe the model of controlling an ensemble of two-level systems with inhomogeneous broadening. In Sec. III, a detailed comparison between the optimization performance using different choices of the function basis is demonstrated. The control field's robustness on unoptimized factors, including variations of field amplitude and environment-induced dephasing, is shown in Sec. IV. In addition, the optimization of a single gate with inhomogeneous broadening and simulations of dynamical decoupling (DD) using our optimization results is presented in Sec. V. In Sec. VI, we conclude our paper with a summary and the prospects of our proposal in QOC.

II. ROBUST ENSEMBLE CONTROL MODEL

Single-spin sensors, such as the nitrogen-vacancy (NV) center in diamond [38,39], with their extraordinarily long coherence times at room temperature [40,41] and their superb operability, e.g., simple initialization and readout by lasers [42], are promising platforms for sensing applications with a high sensitivity and resolution [42–50]. Here, in scenarios such as wide-field sensing [51,52] or vector magnetometry [53–55], ensembles of NV centers are suitably qualified for the performance of these tasks. However, due

to the fact that each NV center may experience a slightly different local environment, an inhomogeneous broadening in the ensembles is inevitable. Similarly, for single spin measurements where the measurement cycle needs to be repeated multiple times, an inhomogeneous broadening in the temporal ensemble is present [56]. Furthermore, the control-field amplitude may also differ between different NV centers in realistic scenarios. These two facts will thereby naturally degrade the fidelity of the control of NV ensembles. In order to overcome these difficulties, QOC methods have been widely adopted [10–12,57,58]. Besides NV-center ensembles, other platforms utilizing ensembles are likewise facing similar difficulties; in the following we therefore focus on generic two-level quantum systems as the target of the QOC.

Driving a single two-level quantum system, with the energy eigenstates $|\downarrow\rangle$ and $|\uparrow\rangle$, from the initial state $|\psi_0\rangle = |\downarrow\rangle$ to the target state $|\psi_g\rangle = |\uparrow\rangle$ in a given time T is, in principle, a simple task that only requires the application of a so-called π pulse. However, due to the aforementioned inhomogeneity present in ensembles, π pulses can only achieve high fidelities for a narrow band of the two-level systems, while leaving the majority of the ensemble poorly controlled [59]. Therefore, the optimization problem we are facing here is the minimization of harmful inhomogeneity effects by engineering an appropriate control field that achieves the best possible overall fidelity for the entire ensemble.

In the laboratory frame, the Hamiltonian that describes a single two-level system of the ensemble under a time-dependent control field $g(t)$ can be written as ($\hbar = 1$)

$$H_{\text{lab}}(t) = \frac{\omega_0 + \delta}{2}\sigma_z + g(t)\sigma_x, \qquad (1)$$

where ω_0 is the energy splitting of the unperturbed spin, δ is the detuning caused by the inhomogeneity, and σ_κ represents Pauli operators, for $\kappa = x, y, z$.

In order to describe the inhomogeneity of the two-level-system ensemble, here, we assume that the detunings δ follow a Gaussian distribution with zero mean value and a standard deviation σ [60,61]. The probability density $p(\delta)$ of the detuning distribution we consider thereby has the form

$$p(\delta) = \frac{1}{\sqrt{2\pi}\sigma}e^{-\frac{\delta^2}{2\sigma^2}}. \qquad (2)$$

In the following, we use the full width at half maximum (FWHM) $W = 2\sqrt{2\ln 2}\sigma$ to quantify the broadness of the distribution. Furthermore, we suppose that the spins which form the two-level systems of the ensemble are spatially sparse, such that their direct interactions can be neglected, which is a valid assumption for an ensemble of NV centers, the direct dipole-dipole interaction of which can usually be discarded [62], due to its rapid decrease with distance.

The performance of the ensemble control field is measured by the expectation value of $f(T, \delta)$ for a given probability density $p(\delta)$ of the detunings, which has the form

$$F = \int d\delta \, p(\delta)f(T, \delta), \qquad (3)$$

where $f(T, \delta) = |\langle\psi_g|\psi(T, \delta)\rangle|^2$ is the fidelity of a final state $|\psi(T, \delta)\rangle$ and the target state for a given control time T and detuning δ. The target of the optimization task is then to

maximize the value of F or to minimize the value of the ensemble infidelity $1 - F$ [29].

III. PHASE-MODULATED CONTROL OPTIMIZATION

A. Method

In order to maximize the value of F, we optimize the parameters that construct the control field $g(t)$ which drives the transition between the two energy eigenstates. Since F is computationally expensive to directly evaluate, we take a small quantity (M) of evenly spaced discrete detunings δ_k, for $k = 1, \ldots, M$, to represent the whole Gaussian distribution [60]. The objective function of the optimization process is then written as

$$F_{\text{obj}} = \mathcal{N} \sum_{k=1}^{M} p(\delta_k) f(\delta_k), \qquad (4)$$

with the normalization constant $\mathcal{N} = [\sum_{k=1}^{M} p(\delta_k)]^{-1}$.

In detail, we use $\delta_k \in [-W, W]$, covering around 98% of the distribution's area, and $M = 15$ to carry out the optimization process using a constrained nonlinear optimization algorithm (Nelder-Mead method) as our optimization solver. In order to evaluate the numerical performance of the optimization methods, we quantify the search speed by the number of objective function evaluations, which we represent by n_f.

Under the same constraints, different choices of the function basis for the control field $g(t)$ show distinct optimization efficiencies. In the widely used SFB the control field has the form

$$g_{\text{SFB}}(t) = \sum_{j=1}^{N} a_j \cos(\omega_j t + \phi_j) \cos(\omega_0 t), \qquad (5)$$

where N is the number of frequency components, while a_j, ω_j, and ϕ_j are the parameters that have to be optimized. It can be seen that the phases ϕ_j are time independent; thus, depending on the number N, the control function $g_s(t)$ can be represented by only several discrete frequencies in Fourier space, which can be rather coarse. In contrast to the SFB, inspired by recently developed Floquet coherent controlling techniques (see, e.g., [63–66]), we introduce a temporal modulation in the phases of the driving field according to

$$g_{\text{PM}}(t) = \sum_{j=1}^{N} a_j \cos\left[\omega_0 t + \frac{b_j}{\nu_j} \sin(\nu_j t)\right], \qquad (6)$$

with a_j, b_j, and ν_j being the optimization parameters. For a better demonstration of the increased frequency involvement in such a scheme, the above equation can be expanded as the Fourier series according to the Jacobi-Anger identity:

$$g_{\text{PM}}(t) = \sum_{j=1}^{N} a_j \sum_{l=-\infty}^{\infty} J_l\left(\frac{b_j}{\nu_j}\right) \cos[(\omega_0 + l\nu_j)t], \qquad (7)$$

where $J_l(x)$ denotes the Bessel function of the lth order. It can be seen that the newly introduced phase modulation enriches the complexity in Fourier space with an infinite number of frequency sidebands the weight of which decreases with the distance from the central frequency ω_0. As we will see, this

feature greatly benefits QOC by making it possible to cover and exploit more frequencies with fewer parameters.

We note that both the SFB and the PM method only involve σ_x components in the laboratory frame; however, in the interaction picture used for the actual optimization, only the PM method will possess both σ_x and σ_y components [see Hamiltonians (11) and (14)]. In order to nevertheless compare the efficiency of the two methods fairly, we further construct two forms of control fields by adding a phase term to the original SFB basis, thus both σ_x and σ_y components will be present in the interaction picture [see Hamiltonians (12) and (13)]. The first is denoted as SFB-P and has the form

$$g_{\text{SFB-P}}(t) = \sum_{j=1}^{N} a_j \cos[\omega_0 t + \omega_j t + \phi_j], \qquad (8)$$

which can be seen as a counterpart of PM and has the optimization parameters a_j, ω_j, and ϕ_j. The other is denoted by SFB-P2, which has a form similar to SFB but one more phase term φ_j, namely,

$$g_{\text{SFB-P2}}(t) = \sum_{j=1}^{N} a_j \cos(\omega_j t + \phi_j) \cos(\omega_0 t + \varphi_j), \qquad (9)$$

with a_j, ω_j, ϕ_j, and φ_j being the optimization parameters.

As we mentioned before, for the sake of convenience, we carry out the numerical optimization in the interaction picture with respect to the central-frequency free Hamiltonian $(\omega_0/2)\sigma_z$. Neglecting counter-rotating terms in a rotating-wave approximation, the transformed laboratory-frame Hamiltonian (1) can be written in the form $H(t) = H_0 + H_\kappa(t)$, with $\kappa = $ SFB, SFB-P, SFB-P2, and PM for the different bases. Here, the drift Hamiltonian is given by

$$H_0 = \frac{\delta}{2} \sigma_z, \qquad (10)$$

and the time-dependent control Hamiltonians read

$$H_{\text{SFB}}(t) = \sum_{j=1}^{N} \frac{a_j}{2} \cos(\omega_j t + \phi_j)\sigma_x, \qquad (11)$$

$$H_{\text{SFB-P}}(t) = \sum_{j=1}^{N} \frac{a_j}{2}[\cos(\omega_j t + \phi_j)\sigma_x + \sin(\omega_j t + \phi_j)\sigma_y], \qquad (12)$$

$$H_{\text{SFB-P2}}(t) = \sum_{j=1}^{N} \frac{a_j}{2} \cos(\omega_j t + \phi_j)[\cos(\varphi_j)\sigma_x + \sin(\varphi_j)\sigma_y], \qquad (13)$$

$$H_{\text{PM}}(t) = \sum_{j=1}^{N} \frac{a_j}{2}\left\{\cos\left[\frac{b_j}{\nu_j}\sin(\nu_j t)\right]\sigma_x + \sin\left[\frac{b_j}{\nu_j}\sin(\nu_j t)\right]\sigma_y\right\} \qquad (14)$$

for the SFB, SFB-P, SFB-P2, and PM methods, respectively. As one sees, all but the control field of the SFB method have both σ_x and σ_y components in the interaction picture.

In practical application there are some constraints imposed on the control fields, that should be taken into account in the optimization. For example, it is impossible to produce arbitrarily strong driving fields. That is, the maximum ampli-
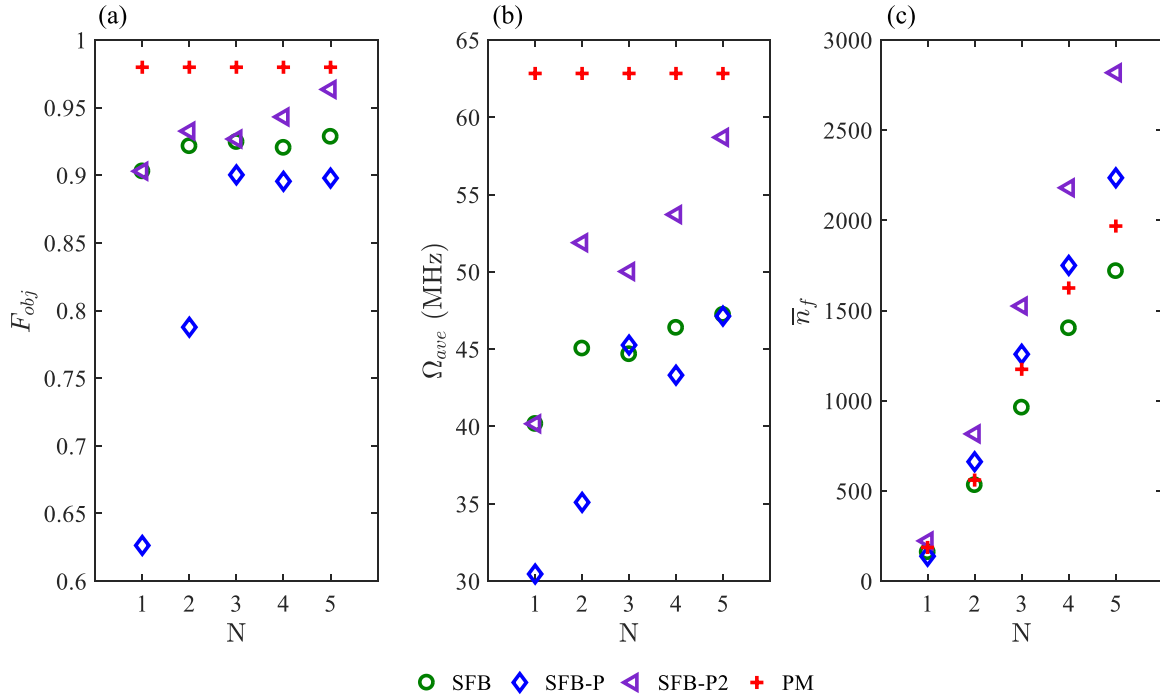
FIG. 1. A comparison of optimal results of SFB, SFB-P, SFB-P2, and PM under the conditions $T = 100$ ns, $W/2\pi = 10$ MHz, and amplitude constraint $\Omega_{max}/2\pi = 10$ MHz. (a) Optimal value of F_{obj} as a function of N. (b) Average field amplitude of the optimal fields as a function of N. (c) Average number of function evaluations over 120 optimal results as a function of N. Under the same constraints, the PM method reaches the best F_{obj} using the least number of parameters, showing the efficiency of the PM method on the premise of limited optimization resources.

tude of the control field in our optimization will be bounded according to $\max |g(t)| \leqslant \Omega_{max}$. Additionally, in practical applications high frequencies are usually not preferable in the applied control fields; thus, all frequency parameters, i.e., ω_k, b_k, and ν_k, are constrained to the range $2\pi \times [0, \ 5/T]$, in terms of the evolution time T. The phase parameters naturally fulfill $\phi_k, \varphi_k \in [0, 2\pi)$. Since a single run of the optimization may result in a local optimal result, i.e., a local minimum in the control-parameter landscape, we always perform 120 runs with different starting points. Then, after the optimal control field is obtained, we randomly generate $K = 10^5$ detunings δ_l obeying the Gaussian distribution (2) in order to approximate the ensemble fidelity by $F \approx \sum_{l=1}^{K} f(\delta_l)/K$.

B. Comparison of the methods

The optimization results of PM, SFB, SFB-P, and SFB-P2 for $T = 100$ ns and $W/2\pi = 10$ MHz under the amplitude constraint $\Omega_{max}/2\pi = 10$ MHz are shown in Fig. 1. We make a comparison of these four methods in terms of three different aspects: the best value of the objective function F_{obj}, the average strength of the optimized control field $\Omega_{ave} = 1/T \int |g(t)| dt$, and the number of function evaluations, which characterizes the search time, all shown as functions of N. Figures 1(a) and 1(b) show a basically positive correlation between F_{obj} and Ω_{ave}, which is in agreement with the common understanding that a stronger manipulation of a system mitigates the effects of noise better. Considering the optimization constraint in the maximum field amplitude Ω_{max}, we may say that the PM method makes better use of the provided

field power. In practice, although there are cases requiring a limited total power of the control field (e.g., in biology environments [67]), the maximal power is the primary limitation of the field generator [60,68], which makes our proposed method reasonable. Figure 1(c) shows the rising trend of the average search time with the increase of N, which is a natural consequence of the expansion of the search space. Here, we use the default maximum number of function evaluations, which equals to $200 \times N_p$, with N_p the number of parameters. Increasing the maximum number of function evaluations could possibly improve the final results at the expense of a prolonged optimization time.

It is noteworthy to mention that, in general, the better efficiency of the PM method is guaranteed on the premise of limited optimization resources, which is a common situation for most realistic optimization tasks. In Fig. 1, the PM method shows its efficiency clearly using only three parameters ($N = 1$) and the shortest searching time while obtaining the largest value of F_{obj}. The optimal value of F_{obj} given by SFB-P2 could merely catch up with PM using 20 parameters ($N = 5$). A comparison between SFB and SFB-P2 implies that introducing the phase term in a proper way can improve the capability of the SFB, as the number of parameters is increased. This could be attributed to the two-directional control field in the interaction picture that the phase term entails, although the inferior performance of SFB-P indicates that this is not always the case.

In order to have a more detailed look into the optimization process, we depict the trajectories of the optimization processes with red lines (PM method) and green lines (SFB-P2
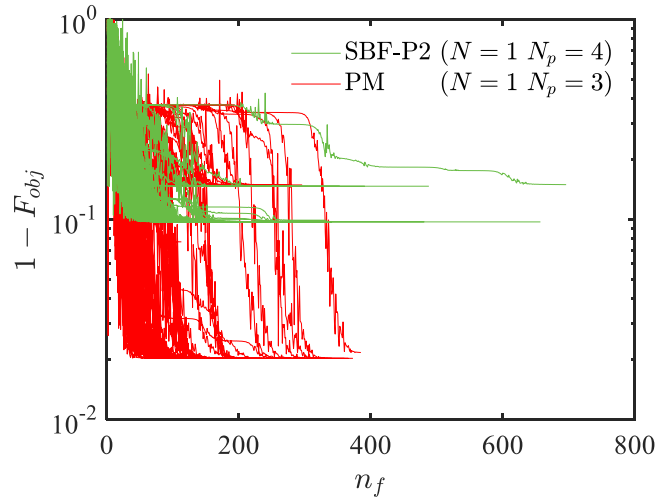
FIG. 2. Infidelity of the final state as a function of the number of objective function evaluations (n_f). Red lines and green lines represent for the PM method with three parameters and the SFB-P2 method with four parameters, respectively, both with 120 different random starting points. The parameters used here are $N = 1$, $T = 100$ ns, $W/2\pi = 10$ MHz, and $\Omega_{max}/2\pi = 10$ MHz.

method) in Fig. 2, both with the same number of basis functions, namely, $N = 1$. It clearly shows the distinct advantages of the PM method, i.e., much better results in relatively shorter searching time. This advantage becomes more prominent as the inhomogeneous broadening become wider, as Fig. 3 displays.

In the following, using PM with $N = 1$ and SFB-P2 with $N = 1$ as well as $N = 5$, we provide a further analysis based on our numerical optimization results. The optimal control fields in the interaction picture are demonstrated in Figs. 4(a)
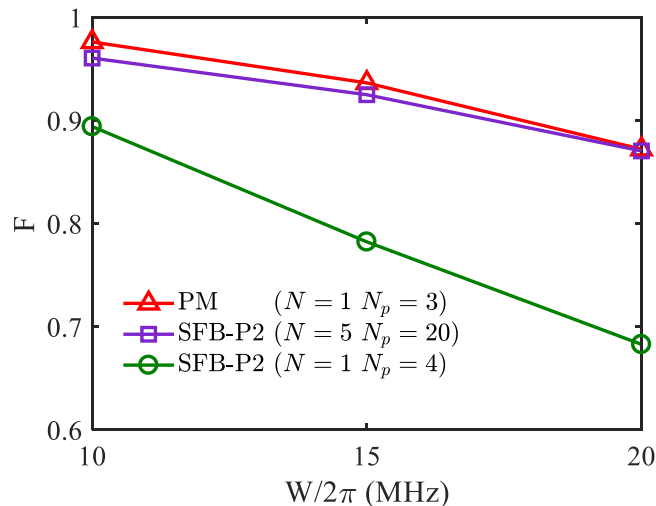

FIG. 3. Optimal fidelity as a function of the FWHM (W) of the distribution of δ. The red line with triangles is the result of the PM method with $N = 1$, $N_p = 3$. The purple line with squares is the result of the SFB-P2 method with $N = 5$, $N_p = 20$. The green line with circles is the result of the SFB-P2 method with $N = 1$, $N_p = 4$. Other parameters used here are $T = 100$ ns, $W/2\pi = 10$ MHz, and $\Omega_{max}/2\pi = 10$ MHz.

and 4(b) for the SFB-P2 and Fig. 4(c) for the PM method, respectively, and the frequency spectra of their control fields in the range [0,50] MHz are shown in Figs. 4(d)–4(f). Figures 4(g)–4(i) show the number of frequency components (counted when the amplitude is higher than 5 MHz) during the optimization process, revealing the potential of the PM method of covering more frequencies with fewer parameters. For SFB-P2, the frequency spectra are the same for the x- and y-directional fields, while for PM this is not the case, due to the property $J_{-l}(x) = (-1)^l J_l(x)$, for $l \in \mathbb{N}$, of the Bessel functions.

Moreover, to explore the stability and convergence of the different methods, Figs. 5(a)–5(c) present 120 results with each method ranked by the value of F_{obj}. For the PM method, more than half of these results reach the best possible value, showing that 120 optimal processes are adequate for PM to obtain the global optimum. In contrast, the distribution of results of SFB-P2 with $N = 5$ shows that 120 processes are not sufficient to guarantee a global optimum. Figures 5(d)–5(f) exhibit the corresponding number of function evaluations for each process (dots) and their average value (solid and dash-dotted lines), reflecting the search time for each optimization method.

As mentioned before, when equipped with a randomization, the PM method obviously belongs to the CRAB family, hence it enriches the toolbox of direct search optimization methods using truncated function bases. In Fig. 5 the results with randomized frequencies (i.e., ω_j and ν_j for SFB-P2 and PM, respectively) are presented using light colors. While the average search times decreased, the best possible value, as well as the distribution of the optimization results, show a disadvantage compared to the unrandomized case. Therefore, for the specific problem we discussed here, a randomization is not necessary. However, it might be found useful and even necessary for other cases.

IV. ROBUSTNESS AGAINST UNOPTIMIZED FACTORS

A. Imperfect control fields

In realistic experiments, variations of the control-field amplitude among different two-level systems in an ensemble are another obstacle which has to be overcome to achieve a high-fidelity control over the ensemble. To describe the influence of the control amplitude variations, we add a linear scaling factor α that amplifies or attenuates the control-field amplitude. Thus, the Hamiltonian (1) is rewritten as

$$H = \frac{\omega_0 + \delta}{2}\sigma_z + \alpha g(t)\sigma_x, \quad (15)$$

where a time-independent scaling factor α is assumed for simplicity.

With the optimized parameters of each method, we obtain the fidelity of a single two-level system under different values of the detuning and the relative amplitude variation factor, as shown in Fig. 6. Comparing Figs. 6(a) and 6(b) [SFB-P2 method] with Fig. 6(c) [PM method], it is apparent that using a similar number of parameters the PM method shows an improved fidelity in a much wider range of the detuning and the control-field variation (for $N = 1$ with a 98% increase of the area where $f > 0.9$ compared to SFB-P2), i.e., again
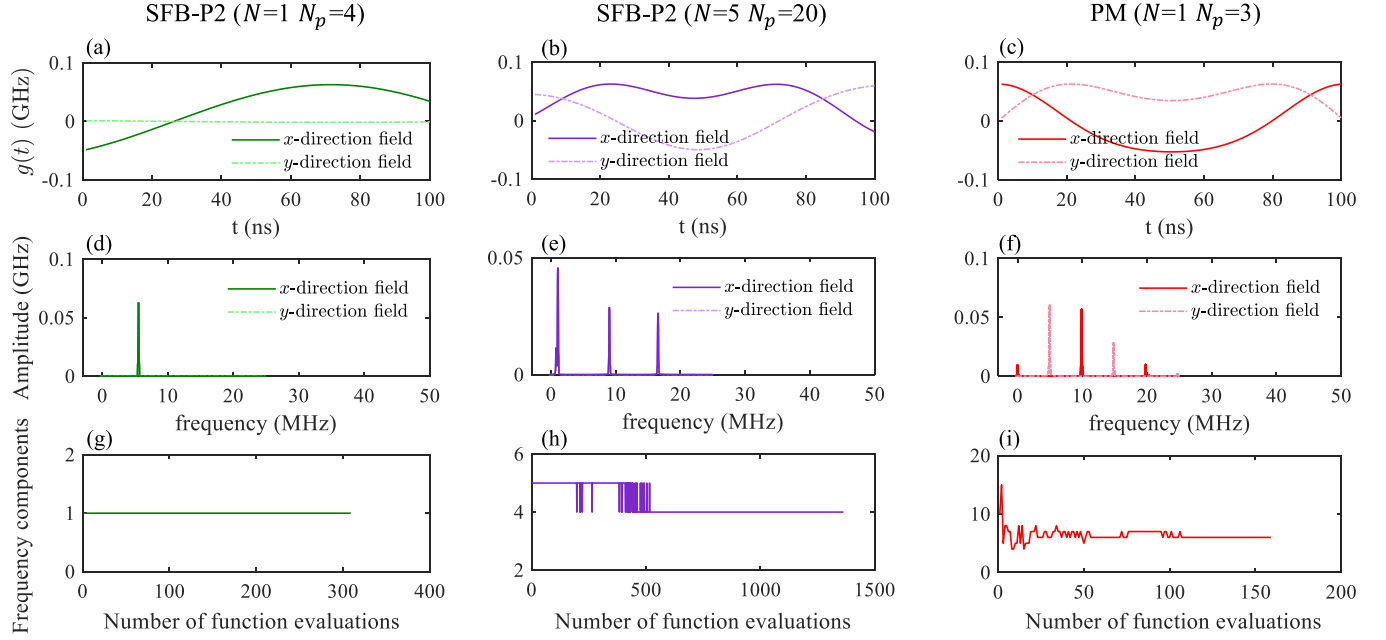
FIG. 4. (a)–(c) Optimal control field in the interaction picture, given by the SFB-P2 ($N = 1$, $N_p = 4$), SFB-P2 ($N = 5$, $N_p = 20$), and PM method ($N = 1$, $N_p = 3$), respectively. Solid line, x-direction field; dot-dashed line, y-direction field. (d)–(f) The corresponding frequency spectrum of the control fields in (a)–(c), respectively. (g)–(i) The corresponding number of frequency components with amplitude $\geqslant 5$ MHz during the optimization process.

showing a stronger robustness, which the SFB-P2 needs at least 20 parameters to reach. A comparison of these methods when the relative amplitude equals to 1 [i.e., a horizontal cut along Figs. 6(a)–6(c)] is also presented in Fig. 6(d). Here, we also show the fidelity for a simple π pulse in the light blue line, viz., for a control Hamiltonian $H_\pi = (\pi/2T)\sigma_x$ in the interaction picture, which suggests all the optimized

results, especially the one from the PM method, show better robustness against inhomogeneities than the π pulse.

B. Effects of noise

In practice, the existence of environmental noise leads to the decoherence of quantum systems. In spin systems, the
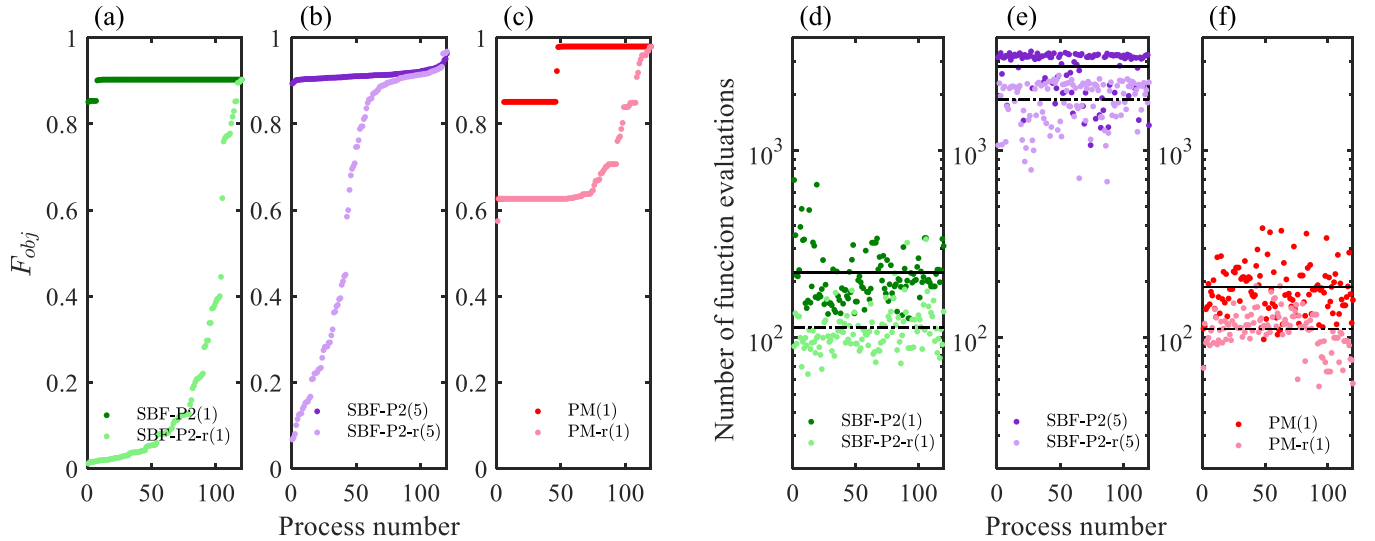

FIG. 5. (a)–(c) Results of 120 optimization processes with different initial values, ranked by the value of F_{obj}. (a) The SFB-P2 method with $N = 1$, $N_p = 4$ and its parameter randomized version SFB-P2-r where ω_i are randomly taken from the range $2\pi \times [0, 5/T]$ and not optimized. (b) The SFB-P2 method with $N = 5$, $N_p = 20$ and its parameter randomized version SFB-P2-r where ω_i are randomly taken from the range $2\pi \times [0, 5/T]$ and not optimized. (c) The PM method with $N = 1$, $N_p = 3$ and its parameter randomized version PM(r) where ν_i are randomly taken from the range $2\pi \times [0, 5/T]$ and not optimized. (d)–(f) Corresponding number of function evaluations (dot) and the average value (solid line, nonrandomized methods; dashed line, randomized methods).
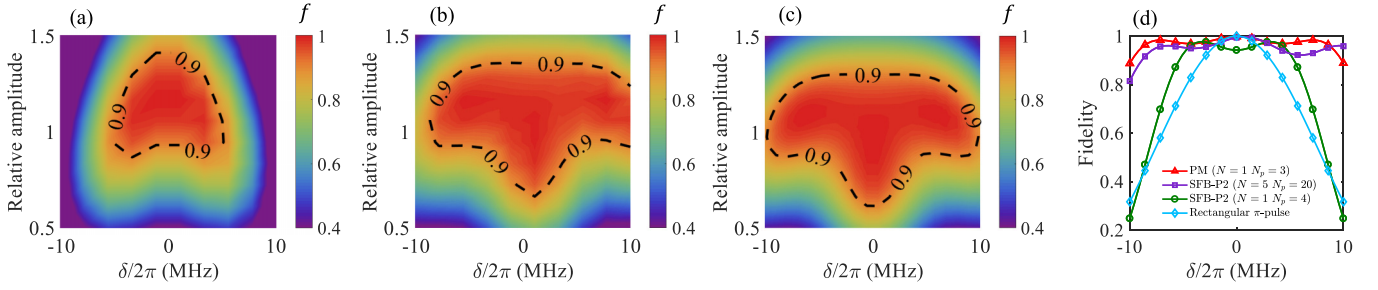
FIG. 6. Fidelity of the final state under different values of the detuning and the relative variations of the control-field amplitude. (a) Results under a control field optimized using the SFB-P2 with $N = 1, N_p = 4$. (b) Results under a control field optimized using the SFB-P2 method with $N = 5, N_p = 20$. (c) Results under a control field optimized using the phase-modulated method with $N = 1, N_p = 3$. (d) A comparison of the three optimal methods and the rectangular π pulse when there are no variations of the control amplitude. The ratio of areas of $f > 0.9$ in (a) and (c) is approximately $1 : 1.98$. The markers in (d) represent the $M = 15$ sample points used in the objective function during the optimization process. Other parameters used here are $T = 100$ ns, $W/2\pi = 10$ MHz, and $\Omega_{\max}/2\pi = 10$ MHz. The amplitude of the rectangular π pulse is $2\pi \times 10$ MHz, with the pulse length of 50 ns.

longitudinal and the transverse relaxation are responsible for the loss of polarization along and perpendicular to the direction of the Pauli operator σ_z, respectively. Considering ensembles of NV centers that can be well described by two-level systems, in the electronic ground-state manifold the energy gap between the $|m_s = 0\rangle$ and the $|m_s = \pm 1\rangle$ states due to the zero-field splitting is roughly 2.8 GHz [38,39], which is much larger than the noise frequencies, which are usually on the order of a few megahertz. This suppresses the longitudinal relaxation and, therefore, we only consider the perpendicular relaxation in the form of pure dephasing, with dephasing times ranging from hundreds of nanoseconds to a few microseconds [49].

Under such pure dephasing, the dynamics of a single two-level system density operator ρ can be described by the Lindblad master equation [56,69]:

$$\frac{\partial}{\partial t}\rho = -i[H, \rho] + \frac{\gamma}{2}(\sigma_z \rho \sigma_z - \rho), \quad (16)$$

where γ is the reciprocal of the dephasing time T_2^*.

For simplicity, we assume that the dephasing rates of each two-level system are equal to the average dephasing rate of the ensemble. Since the final state evolved under noise is generally a mixed state, which is described by the density operator $\rho(T, \delta)$, the fidelity between the final state and the target state has to be written as

$$f(\delta) = \langle \psi_g | \rho(T, \delta) | \psi_g \rangle. \quad (17)$$

In Fig. 7, we show the average fidelity F using control fields optimized under the PM and the SFB-P2 method, respectively, as a function of the dephasing rate γ. One can clearly see that, not surprisingly, the fidelity decreases as the dephasing rate becomes larger. However, under reasonable noise levels, e.g., up to 2 MHz for NV-center ensembles, the achieved fidelity is still sufficiently high to be applicable. Also, under dephasing noise, the PM results surpass the SFB-P2 method results, showing a better robustness against noise. Additionally, the robustness against detuning and control-field variations under dephasing noise is depicted in Fig. 8. Compared to their nondephasing counterparts in Fig. 6, the $f > 0.9$ area shrinks while maintaining similar profiles. The ratio of $f > 0.9$ areas of PM and SFB-P2 ($N = 1$) is $1.74 : 1$, approximately.

V. GATE SYNTHESIS AND DYNAMICAL DECOUPLING

The above optimization of state transitions can be easily extended to produce robust single qubit gates by replacing the state fidelity with the gate fidelity

$$f_g(\delta) = \frac{1}{2} + \frac{1}{3} \sum_{\kappa=x,y,z} \text{Tr}\left(U \frac{\sigma_\kappa}{2} U^\dagger U_\delta \frac{\sigma_\kappa}{2} U_\delta^\dagger \right) \quad (18)$$

in a two-level system [70,71], where U is the target gate and

$$U_\delta = \mathcal{T} \exp\left[-i \int_0^t H(\delta, t') dt' \right] \quad (19)$$

is the unitary evolution operator, with $\mathcal{T}$ being the time-ordering operator.

Under inhomogeneous broadening, the objective function is then written as

$$F_{\text{obj}}^G = \mathcal{N} \sum_{k=1}^{M} p(\delta_k) f_g(\delta_k), \quad (20)$$
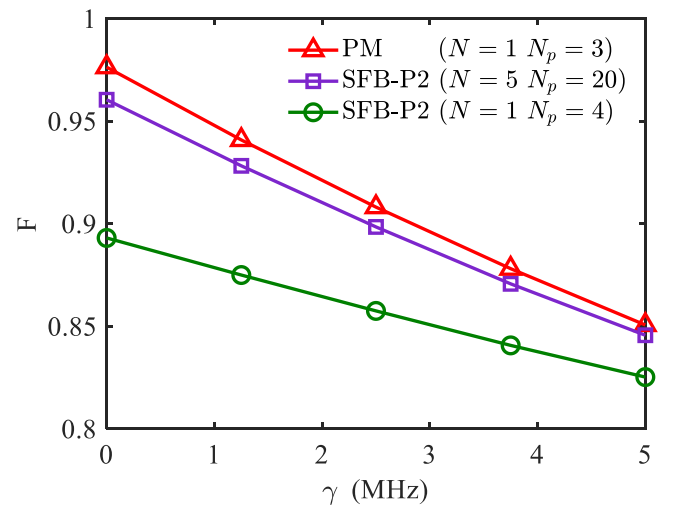

FIG. 7. Average fidelity F of the ensemble system as a function of the dephasing rate, using the same optimized control fields as in Fig. 6.
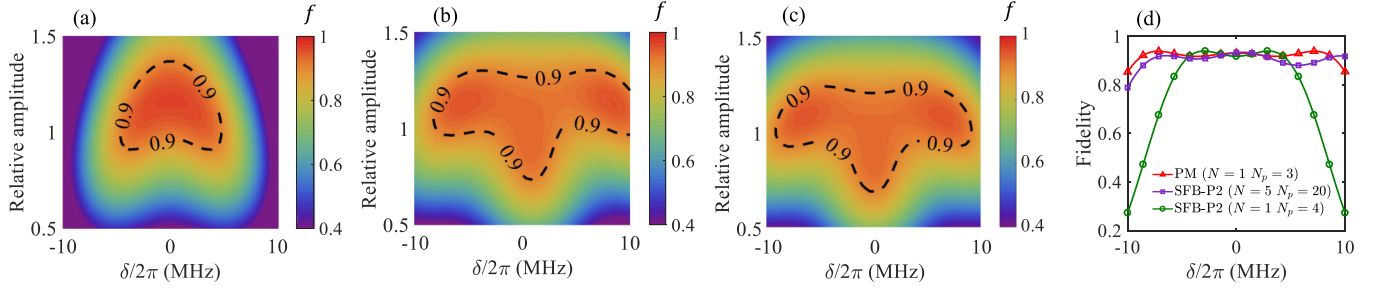
FIG. 8. Fidelity of the final state with dephasing rate $\gamma = 2$ MHz, using the same control fields and parameters as in Fig. 6. (a) Results under a control field optimized using the SFB-P2 with $N = 1$, $N_p = 4$. (b) Results under a control field optimized using the SFB-P2 method with $N = 5$, $N_p = 20$. (c) Results under a control field optimized using the PM method with $N = 1$, $N_p = 3$. (d) A comparison of the three optimal methods when there are no variations of the control amplitude. The ratio of areas of $f > 0.9$ in (a) and (c) is approximately 1 : 1.74. The markers in (d) represent the $M = 15$ sample points used in the objective function during the optimization process.

where $\mathcal{N}$ and $p(\delta_k)$ take the same form as those in Eq. (4). The optimized results of the PM ($N = 1, 2$) and SFB-P2 ($N = 1, 5$) methods with the Hadamard gate and the Pauli-X, Pauli-Y, and Pauli-Z gates are shown in Fig. 9. The parameters used in the optimization process are $T = 100$ ns, $W/2\pi = 10$ MHz, and $\Omega_{\max}/2\pi = 10$ MHz. Compared with the SFB-P2, the PM method no longer shows absolute superiority (e.g., for the Pauli-Y gate), but still shows its utility in view of versatility for different gate types and resource economies.

The robustness of the optimized control field under detunings and field amplitude variations is further demonstrated in Fig. 10. Compared with the rectangular pulse with the same maximal amplitude, optimized pulses given by the PM method show a general better robustness, although the degree of improvement is less obvious compared with the state transition case in Fig. 6(d).

Single qubit gates are the fundamental tools for DD [72] and nuclear spin detection [73,74]. The most widely used DD

FIG. 9. Optimal results of the robust gate fidelity given by PM ($N = 1, 2$) and SFB-P2 ($N = 1, 5$) methods, with the targeted Hadamard gate, Pauli-X gate, Pauli-Y gate, and Pauli-Z gate, respectively. Here we use $K = 10^5$ random detunings δ_l obeying the Gaussian distribution (2) with $W/2\pi = 10$ MHz, to approximate the ensemble fidelity by $F_G \approx \sum_{l=1}^{K} f_g(\delta_l)/K$. Parameters used in the optimization process are $T = 100$ ns, $W/2\pi = 10$ MHz, and $\Omega_{\max}/2\pi = 10$ MHz.

techniques, including the Carr-Purcell sequence [75] and the XY family sequence [76], play important roles in eliminating the effects of environmental noise. In Fig. 11, we give a simulation of the spin coherence time T_2 using one XY8 pulse sequence implemented using the PM optimal field and a rectangular π pulse, respectively. The drift Hamiltonian of the system in the interaction picture is

$$H_{dr}(t) = \frac{\delta + \delta_d(t)}{2}\sigma_z, \quad (21)$$

with a constant component of noise δ following a Gaussian distribution, and a dynamic Lorentzian noise $\delta_d(t)$, which is modeled as an Ornstein-Uhlenbeck process and approximated by [77]

$$\delta_d(t + \Delta t) = \delta_d(t)e^{-\Delta t/\tau} + \left[\frac{c\tau}{2}\left(1 - e^{-2\Delta t/\tau}\right)\right]^{1/2}n, \quad (22)$$

with τ and c being the correlation time and diffusion constant of the noise, respectively, and n representing a sample value of the unit normal distribution. We take the static noise δ following a Gaussian distribution with a zero mean value and FWHM of $2\pi \times 26.5$ MHz ($T_2^* \approx 20$ ns), and the dynamic noise $\delta_d(t)$ with $\tau = 20$ μs and the standard deviation $\sqrt{c\tau/2} = 2\pi \times 50$ KHz [78].

Due to the finite pulse length of the control field, the effect of noise cannot be neglected during the pulse; thus, the total Hamiltonian in this period is

$$H(t) = H_{dr}(t) + H_c(t), \quad (23)$$

where $H_c(t)$ takes the form of Eq. (14) for the PM control field and the constant form $(\pi/2T_{\text{pulse}})\sigma_{x(y)}$ for the rectangular Pauli-X (Y) pulse, with T_{pulse} the pulse length. We use the phase-modulated method with $N = 1$, $W/2\pi = 26.5$ MHz, and $\Omega_{\max}/2\pi = 10$ MHz to optimize the Pauli-X and Pauli-Y gates in an XY-8 sequence with pulse length $T_{\text{pulse}} = 100$ ns, and the pulse length of the rectangular pulse for the standard XY-8 sequence is set to be $T_{\text{pulse}} = 50$ ns, such that the two kinds of pulses have the same maximal amplitude. The pulse interval is $\tau_{\text{pulse}} \in [0.4, 5.6]$ μs for the PM pulses and $\tau_{\text{pulse}} \in [0.45, 5.65]$ μs for the rectangular pulses, such that the total evolution time T for both methods is $T \in [4, 45.6]$ μs.

The simulated coherence time using the PM optimal fields is $T_2 \approx 39$ μs, thereby increasing the $T_2 \approx 24$ μs using rectangular pulses by roughly one-half. We note that the
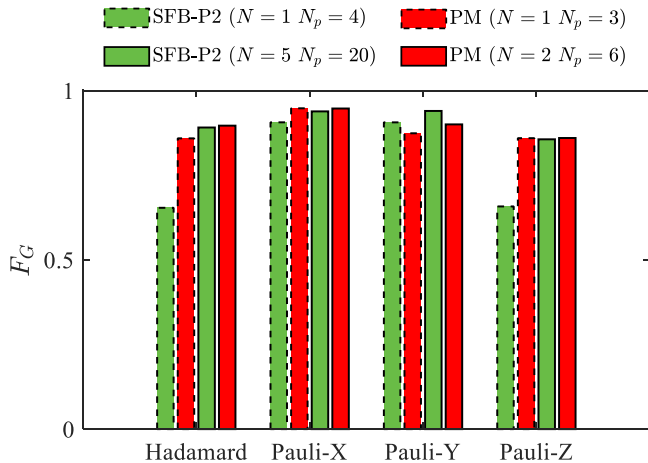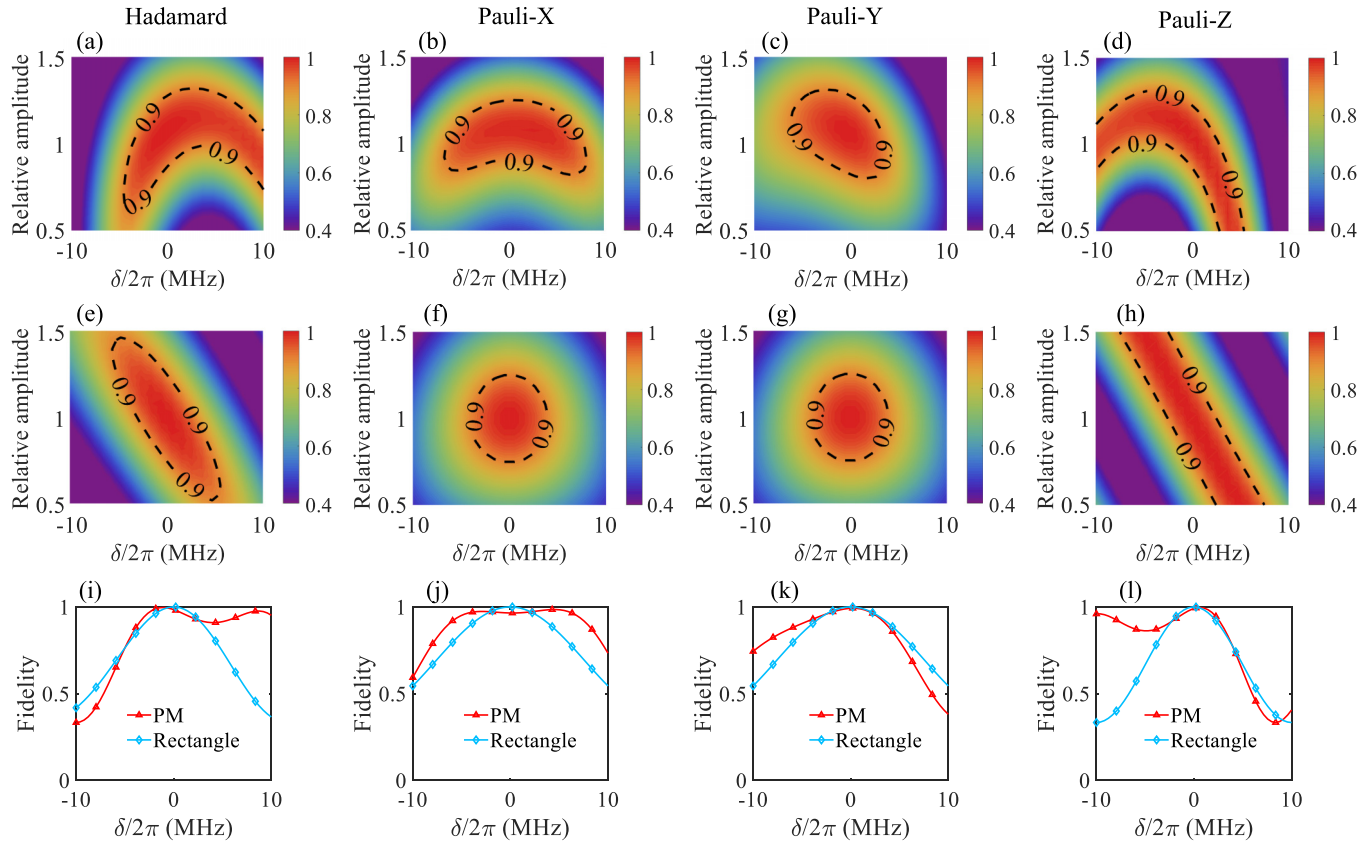
FIG. 10. Gate fidelity under different values of the detuning and the relative variations of the control-field amplitude. (a)–(d) Results of the control fields optimized using the phase modulated method with $N = 2$, with the target gate being the Hadamard gate, Pauli-X gate, Pauli-Y gate, and Pauli-Z gate, respectively. Parameters used in the optimization process are $T = 100$ ns, $W/2\pi = 10$ MHz, and $\Omega_{max}/2\pi = 10$ MHz. (e)–(h) Results of the standard rectangular pulse with amplitude $2\pi \times 10$ MHz and pulse length 50 ns, with the target gate being the Hadamard gate, Pauli-X gate, Pauli-Y gate, and Pauli-Z gate, respectively. (i)–(l) A comparison of the optimized PM pulse and the rectangular pulse when there are no variations of the control amplitude.

SFB-P2 method with a similar number of parameters will likewise give good results in such simulations and is also worth investigating for further application, where the two methods could be combined in order to complement each other. With further exploration and more target designs, the PM method as well as the SFB-P2 method can be used to enhance the robustness of DD sequences in different scenarios and thus have a high potential to be applied in quantum sensing experiments for an improvement of the detection precision.

VI. CONCLUSION

We have introduced a direct-optimization method based on a PM function basis that is feasible for applications in robust quantum control problems. As an example, we apply this method to find robust control fields for the control of an ensemble of two-level systems exhibiting an inhomogeneous broadening. Constrained by the same maximal field strength and the same maximal search resources, the PM method reaches highly improved results compared with the widely used SFB and comparable results with the phase-introduced standard Fourier basis (SFB-P2), using one order of magnitude less optimization time. A detailed analysis of the overall optimization results further reveals that the PM method shows a stable capability to find the global optimum in the parameter

landscape with comparable or lower search resources, while SFB-P2 with more parameters is unable to plausibly obtain the same results in every trial run with the same search resources. A significant advantage of our PM method is the involvement of multiple frequency components in a single element of the PM function basis. This is shown in the frequency spectrum of the control fields during the optimization process. Considering possible drifts of the control-field amplitudes and decoherence noise, when applied in a realistic model of an ensemble system, the PM method also shows a significantly stronger robustness in both of these situations, compared with the SFB-P2 method in the same low-dimensional parameter space. As a further example, we also demonstrate the utilization of the PM function basis in the optimization of robust gate control fields for dynamical decoupling, leading to a prolonged coherence time of the system compared to traditional rectangular pulses.

We note that while the results we present in this paper are produced using a direct search optimization solver based on the Nelder-Mead method, similar results can also be obtained using a gradient-based solver. This implies that the relative advantage of the PM method over SFB methods relies on the form of basis rather than the specific solver, and can thereby be utilized beyond a direct search optimization. For the specific problem we discussed in this paper, the use of randomization of some parameters is not recommended since
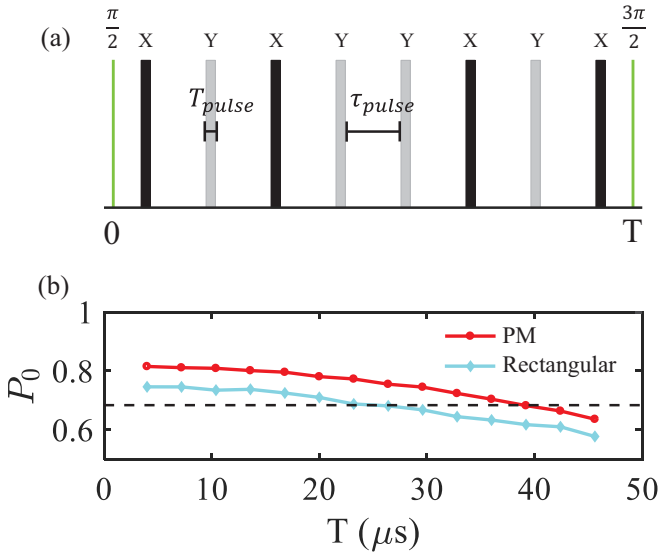
FIG. 11. Simulation of the coherence time T_2 using one XY8 series. The initial state is taken as $\psi_0 = |0\rangle$. (a) Schematic pulse location during one simulation process with evolution time T. The slim green lines at the beginning and the end represent the initialization pulse rotating the state around the X axis by $\pi/2$ and the readout pulse rotating the state around the X axis by $3\pi/2$, respectively, where both are presumed to be instantaneous. The black and gray sticks represent Pauli-X and Pauli-Y gates in the XY8 series, respectively, with finite pulse length T_{pulse}. The pulse separation τ_{pulse} refers to the time period from the end of one pulse to the beginning of the next pulse. The pulse number and pulse length are fixed for different evolution times T, and T_2 is recognized as the value of T at which the population of $|0\rangle$ drops to $(1 + 1/e)/2$. (b) The population P_0 of $|0\rangle$ as a function of T. Each point averages the results of 1200 evolutions. PM optimal control fields give $T_2 \approx 39$ μs, improving the coherence time with rectangular pulse $T_2 \approx 24$ μs by half.

it degrades the probability of finding the global optimum. However, applying the randomization of parameters to the PM method is nevertheless worth considering and might be useful in other contexts.

With short optimization times and a strong robustness, the proposed PM method provides a potentially superior gradient-free optimization method. It has a high potential value in the field of spin-ensemble manipulations and optimal control in many-body physics, where the expensive evaluation process of the objective functions makes the total optimization process time consuming, as the parameter space expands quickly with the system size. Furthermore, our proposed method can be straightforwardly adapted and integrated to advanced and highly developed optimization packages, e.g., remote dressed chopped random-basis (RedCRAB) optimization algorithm, which is capable of performing closed-loop optimization remotely [79], and has been recently used to experimentally demonstrate the generation of genuine multipartite entanglement in the form of 20-qubit Greenberger-Horne-Zeilinger states with Rydberg atoms [80]. In addition, the capabilities to conveniently optimize gate robustness and prolong the coherence time using XY-8 sequences make the PM method potentially useful for improving the performance of DD techniques under inhomogeneous broadening [81] and quantum sensing experiments [78].

[1] E. Räsänen, A. Castro, J. Werschnik, A. Rubio, and E. K. U. Gross, Optimal Control of Quantum Rings by Terahertz Laser Pulses, Phys. Rev. Lett. **98**, 157404 (2007).

[2] A. Carlini, A. Hosoya, T. Koike, and Y. Okudaira, Time-Optimal Quantum Evolution, Phys. Rev. Lett. **96**, 060503 (2006).

[3] U. Hohenester, P. K. Rekdal, A. Borzì, and J. Schmiedmayer, Optimal quantum control of Bose-Einstein condensates in magnetic microtraps, Phys. Rev. A **75**, 023602 (2007).

[4] G. Turinici and H. Rabitz, Wavefunction controllability for finite-dimensional bilinear quantum systems, J. Phys. A **36**, 2565 (2003).

[5] T. C. Weinacht, J. Ahn, and P. H. Bucksbaum, Controlling the shape of a quantum wavefunction, Nature (London) **397**, 233 (1999).

[6] M. D. Lang and C. M. Caves, Optimal quantum-enhanced interferometry, Phys. Rev. A **90**, 025802 (2014).

[7] G. Gordon, G. Kurizki, and D. A. Lidar, Optimal Dynamical Decoherence Control of a Qubit, Phys. Rev. Lett. **101**, 010403 (2008).

[8] L. Dong, H. Liang, C.-K. Duan, Y. Wang, Z. Li, X. Rong, and J. Du, Optimal control of a spin bath, Phys. Rev. A **99**, 013426 (2019).

[9] Y.-H. Ji, J.-j. Hu, J.-H. Huang, and Q. Ke, Optimal control-based states transfer for non-Markovian quantum system, Physica E **81**, 77 (2016).

[10] N. Khaneja, T. Reiss, C. Kehlet, T. Schulte-Herbrüggen, and S. J. Glaser, Optimal control of coupled spin dynamics: Design of NMR pulse sequences by gradient ascent algorithms, J. Magn. Reson. **172**, 296 (2005).

[11] J. Scheuer, X. Kong, R. S. Said, J. Chen, A. Kurz, L. Marseglia, J. Du, P. R. Hemmer, S. Montangero, T. Calarco, B. Naydenov, and F. Jelezko, Precise qubit control beyond the rotating wave approximation, New J. Phys. **16**, 093022 (2014).

[12] F. Dolde, V. Bergholm, Y. Wang, I. Jakobi, B. Naydenov, S. Pezzagna, J. Meijer, F. Jelezko, P. Neumann, T. Schulte-Herbrüggen, J. Biamonte, and J. Wrachtrup, High-fidelity spin entanglement using optimal control, Nat. Commun. **5**, 3371 (2014).

[13] J. Kelly, R. Barends, B. Campbell, Y. Chen, Z. Chen, B. Chiaro, A. Dunsworth, A. G. Fowler, I.-C. Hoi, E. Jeffrey, A. Megrant, J. Mutus, C. Neill, P. J. J. O'Malley, C. Quintana, P. Roushan, D. Sank, A. Vainsencher, J. Wenner, T. C. White, A. N. Cleland, and J. M. Martinis, Optimal Quantum Control Using Randomized Benchmarking, Phys. Rev. Lett. **112**, 240504 (2014).

[14] S. Montangero, T. Calarco, and R. Fazio, Robust Optimal Quantum Gates for Josephson Charge Qubits, Phys. Rev. Lett. **99**, 170501 (2007).

[15] M. Amy, D. Maslov, M. Mosca, and M. Roetteler, A meet-in-the-middle algorithm for fast synthesis of depth-optimal quantum circuits, IEEE Trans. Comput.-Aided Des. Integr. Circuits Syst. **32**, 818 (2013).

[16] D. J. Egger and F. K. Wilhelm, Adaptive Hybrid Optimal Quantum Control for Imprecisely Characterized Systems, Phys. Rev. Lett. **112**, 240503 (2014).

[17] T. Choi, S. Debnath, T. A. Manning, C. Figgatt, Z.-X. Gong, L.-M. Duan, and C. Monroe, Optimal Quantum Control of Multimode Couplings between Trapped Ion Qubits for Scalable Entanglement, Phys. Rev. Lett. **112**, 190502 (2014).

[18] R. Nair and B. J. Yen, Optimal Quantum States for Image Sensing in Loss, Phys. Rev. Lett. **107**, 193602 (2011).

[19] S. J. Glaser, U. Boscain, T. Calarco, C. P. Koch, W. Köckenberger, R. Kosloff, I. Kuprov, B. Luy, S. Schirmer, T. Schulte-Herbrüggen, D. Sugny, and F. K. Wilhelm, Training Schrödinger's cat: Quantum optimal control, Eur. Phys. J. D **69**, 279 (2015).

[20] M. Jiang, J. Bian, X. Liu, H. Wang, Y. Ji, B. Zhang, X. Peng, and J. Du, Numerical optimal control of spin systems at zero magnetic field, Phys. Rev. A **97**, 062118 (2018).

[21] G. Jäger, D. M. Reich, M. H. Goerz, C. P. Koch, and U. Hohenester, Optimal quantum control of Bose-Einstein condensates in magnetic microtraps: Comparison of gradient-ascent-pulse-engineering and Krotov optimization schemes, Phys. Rev. A **90**, 033628 (2014).

[22] P. de Fouquieres, S. G. Schirmer, S. J. Glaser, and I. Kuprov, Second order gradient ascent pulse engineering, J. Magn. Reson. **212**, 412 (2011).

[23] J. Tian, T. Du, Y. Liu, H. Liu, F. Jin, R. S. Said, and J. Cai, Optimal quantum optical control of spin in diamond, Phys. Rev. A **100**, 012110 (2019).

[24] V. Krotov, *Global Methods in Optimal Control Theory* (CRC, Boca Raton, FL, 1995), Vol. 195.

[25] Y. Maday, J. Salomon, and G. Turinici, Monotonic time-discretized schemes in quantum control, Numer. Math. **103**, 323 (2006).

[26] D. M. Reich, M. Ndong, and C. P. Koch, Monotonically convergent optimization in quantum control using Krotov's method, J. Chem. Phys. **136**, 104103 (2012).

[27] R. Eitan, M. Mundt, and D. J. Tannor, Optimal control with accelerated convergence: Combining the Krotov and quasi-Newton methods, Phys. Rev. A **83**, 053426 (2011).

[28] J. J. W. H. Sørensen, M. O. Aranburu, T. Heinzel, and J. F. Sherson, Quantum optimal control in a chopped basis:

[29] Applications in control of Bose-Einstein condensates, Phys. Rev. A **98**, 022119 (2018).

[29] T. Caneva, T. Calarco, and S. Montangero, Chopped random-basis quantum optimization, Phys. Rev. A **84**, 022326 (2011).

[30] P. Doria, T. Calarco, and S. Montangero, Optimal Control Technique for Many-Body Quantum Dynamics, Phys. Rev. Lett. **106**, 190501 (2011).

[31] K. Jachymski, Z. Idziaszek, and T. Calarco, Fast Quantum Gate via Feshbach-Pauli Blocking in a Nanoplasmonic Trap, Phys. Rev. Lett. **112**, 250502 (2014).

[32] N. Rach, M. M. Müller, T. Calarco, and S. Montangero, Dressing the chopped-random-basis optimization: A bandwidth-limited access to the trap-free landscape, Phys. Rev. A **92**, 062343 (2015).

[33] J.-S. Li, J. Ruths, and D. Stefanatos, A pseudospectral method for optimal control of open quantum systems, J. Chem. Phys. **131**, 164110 (2009).

[34] D. Stefanatos and E. Paspalakis, Efficient generation of the triplet Bell state between coupled spins using transitionless quantum driving and optimal control, Phys. Rev. A **99**, 022327 (2019).

[35] S. Machnes, E. Assémat, D. Tannor, and F. K. Wilhelm, Tunable, Flexible, and Efficient Optimization of Control Pulses for Practical Qubits, Phys. Rev. Lett. **120**, 150401 (2018).

[36] B. Russell and H. Rabitz, Common foundations of optimal control across the sciences: Evidence of a free lunch, Phil. Trans. R. Soc. A **375**, 20160210 (2017).

[37] F. Frank, J. Unden, Thomas abd Zoller, R. S. Said, T. Calarco, S. Montangero, B. Naydenov, and F. Jelezko, Autonomous calibration of single spin qubit operations, npj Quantum Inf. **3**, 48 (2017).

[38] F. Jelezko and J. Wrachtrup, Single defect centres in diamond: A review, Phys. Stat. Sol. **203**, 3207 (2006).

[39] M. W. Doherty, N. B. Manson, P. Delaney, F. Jelezko, J. Wrachtrup, and L. C. Hollenberg, The nitrogen-vacancy colour centre in diamond, Phys. Rep. **528**, 1 (2013).

[40] G. Balasubramanian, P. Neumann, D. Twitchen, M. Markham, R. Kolesov, N. Mizuochi, J. Isoya, J. Achard, J. Beck, J. Tissler, V. Jacques, P. R. Hemmer, F. Jelezko, and J. Wrachtrup, Ultralong spin coherence time in isotopically engineered diamond, Nat. Mater. **8**, 383 (2009).

[41] P. C. Maurer, G. Kucsko, C. Latta, L. Jiang, N. Y. Yao, S. D. Bennett, F. Pastawski, D. Hunger, N. Chisholm, M. Markham, D. J. Twitchen, J. I. Cirac, and M. D. Lukin, Room-temperature quantum bit memory exceeding one second, Science **336**, 1283 (2012).

[42] A. Gruber, A. Dräbenstedt, C. Tietz, L. Fleury, J. Wrachtrup, and C. von Borczyskowski, Scanning confocal optical microscopy and magnetic resonance on single defect centers, Science **276**, 2012 (1997).

[43] F. Jelezko, T. Gaebel, I. Popa, A. Gruber, and J. Wrachtrup, Observation of Coherent Oscillations in a Single Electron Spin, Phys. Rev. Lett. **92**, 076401 (2004).

[44] J. R. Maze, P. L. Stanwix, J. S. Hodges, S. Hong, J. M. Taylor, P. Cappellaro, L. Jiang, M. V. G. Dutt, E. Togan, A. S. Zibrov, A. Yacoby, R. L. Walsworth, and M. D. Lukin, Nanoscale magnetic sensing with an individual electronic spin in diamond, Nature (London) **455**, 644 (2008).

[45] G. Balasubramanian, I. Y. Chan, R. Kolesov, M. Al-Hmoud, J. Tisler, C. Shin, C. Kim, A. Wojcik, P. R. Hemmer, A. Krueger,

T. Hanke, A. Leitenstorfer, R. Bratschitsch, F. Jelezko, and J. Wrachtrup, Nanoscale imaging magnetometry with diamond spins under ambient conditions, Nature (London) **455**, 648 (2008).

[46] M. S. Grinolds, S. Hong, P. Maletinsky, L. Luan, M. D. Lukin, R. L. Walsworth, and A. Yacoby, Nanoscale magnetic imaging of a single electron spin under ambient conditions, Nat. Phys. **9**, 215 (2013).

[47] C. Müller, X. Kong, J. M. Cai, K. Melentijević, A. Stacey, M. Markham, D. Twitchen, J. Isoya, S. Pezzagna, J. Meijer, J. F. Du, M. B. Plenio, B. Naydenov, L. P. McGuinness, and F. Jelezko, Nuclear magnetic resonance spectroscopy with single spin sensitivity, Nat. Commun. **5**, 4703 (2014).

[48] F. Shi, Q. Zhang, P. Wang, H. Sun, J. Wang, X. Rong, M. Chen, C. Ju, F. Reinhard, H. Chen, J. Wrachtrup, J. Wang, and J. Du, Single-protein spin resonance spectroscopy under ambient conditions, Science **347**, 1135 (2015).

[49] R. Schirhagl, K. Chang, M. Loretz, and C. L. Degen, Nitrogen-vacancy centers in diamond: Nanoscale sensors for physics and biology, Annu. Rev. Phys. Chem. **65**, 83 (2014).

[50] J. Cai, F. Jelezko, and M. B. Plenio, Hybrid sensors based on color centres in diamond and piezoactive layers, Nat. Commun. **5**, 4065 (2014).

[51] L. M. Pham, D. Le Sage, P. L. Stanwix, T. K. Yeung, D. Glenn, A. Trifonov, P. Cappellaro, P. R. Hemmer, M. D. Lukin, H. Park, A. Yacoby, and R. L. Walsworth, Magnetic field imaging with nitrogen-vacancy ensembles, New J. Phys. **13**, 045021 (2011).

[52] D. Le Sage, K. Arai, D. R. Glenn, S. J. DeVience, L. M. Pham, L. Rahn-Lee, M. D. Lukin, A. Yacoby, A. Komeili, and R. L. Walsworth, Optical magnetic imaging of living cells, Nature (London) **496**, 486 (2013).

[53] J. M. Schloss, J. F. Barry, M. J. Turner, and R. L. Walsworth, Simultaneous Broadband Vector Magnetometry Using Solid-State Spins, Phys. Rev. Appl. **10**, 034044 (2018).

[54] S. Steinert, F. Dolde, P. Neumann, A. Aird, B. Naydenov, G. Balasubramanian, F. Jelezko, and J. Wrachtrup, High sensitivity magnetic imaging using an array of spins in diamond, Rev. Sci. Instrum. **81**, 043705 (2010).

[55] H. Clevenson, L. M. Pham, C. Teale, K. Johnson, D. Englund, and D. Braje, Robust high-dynamic-range vector magnetometry with nitrogen-vacancy centers in diamond, Appl. Phys. Lett. **112**, 252406 (2018).

[56] W. Yang, W.-L. Ma, and R.-B. Liu, Quantum many-body theory for electron spin decoherence in nanoscale nuclear spin baths, Rep. Prog. Phys. **80**, 016001 (2016).

[57] D. Daems, A. Ruschhaupt, D. Sugny, and S. Guérin, Robust Quantum Control by a Single-Shot Shaped Pulse, Phys. Rev. Lett. **111**, 050404 (2013).

[58] J. Zeng and E. Barnes, Fastest pulses that implement dynamically corrected single-qubit phase gates, Phys. Rev. A **98**, 012301 (2018).

[59] B. Bartels, Smooth optimal control of coherent quantum dynamics, Ph.D. thesis, Albert-Ludwigs-Universität Freiburg, 2015.

[60] T. Nöbauer, A. Angerer, B. Bartels, M. Trupke, S. Rotter, J. Schmiedmayer, F. Mintert, and J. Majer, Smooth Optimal Quantum Control for Robust Solid-State Spin Magnetometry, Phys. Rev. Lett. **115**, 190801 (2015).

[61] A. Vagov, V. M. Axt, and T. Kuhn, Impact of pure dephasing on the nonlinear optical response of single quantum dots and dot ensembles, Phys. Rev. B **67**, 115338 (2003).

[62] S. D. Bennett, N. Y. Yao, J. Otterbach, P. Zoller, P. Rabl, and M. D. Lukin, Phonon-Induced Spin-Spin Interactions in Diamond Nanostructures: Application to Spin Squeezing, Phys. Rev. Lett. **110**, 156402 (2013).

[63] A. Russomanno and G. E. Santoro, Floquet resonances close to the adiabatic limit and the effect of dissipation, J. Stat. Mech. Theor. Exp. (2017) 103104.

[64] Z. Shu, Y. Liu, Q. Cao, P. Yang, S. Zhang, M. B. Plenio, F. Jelezko, and J. Cai, Observation of Floquet Raman Transition in a Driven Solid-State Spin System, Phys. Rev. Lett. **121**, 210501 (2018).

[65] A. P. Saiko, S. A. Markevich, and R. Fedaruk, Bloch–Siegert oscillations in the Rabi model with an amplitude-modulated driving field, Laser Phys. **29**, 124004 (2019).

[66] S. Bertaina, H. Vezin, H. D. Raedt, and I. Chiorescu, Experimental protection of quantum coherence by using a phase-tunable image drive, arXiv:2001.02417.

[67] Q.-Y. Cao, P.-C. Yang, M.-S. Gong, M. Yu, A. Retzker, M. B. Plenio, C. Müller, N. Tomek, B. Naydenov, L. P. McGuinness, F. Jelezko, and J.-M. Cai, Protecting Quantum Spin Coherence of Nanodiamonds in Living Cells, Phys. Rev. Appl. **13**, 024021 (2020).

[68] R. Bowler, U. Warring, J. W. Britton, B. C. Sawyer, and J. Amini, Arbitrary waveform generator for quantum information processing with trapped ions, Rev. Sci. Instrum. **84**, 033108 (2013).

[69] H.-P. Breuer and F. Petruccione, *The Theory of Open Quantum Systems* (Oxford University, New York, 2002).

[70] M. D. Bowdrey, D. K. Oi, A. J. Short, K. Banaszek, and J. A. Jones, Fidelity of single qubit maps, Phys. Lett. A **294**, 258 (2002).

[71] M. A. Nielsen, A simple formula for the average gate fidelity of a quantum dynamical operation, Phys. Lett. A **303**, 249 (2002).

[72] L. Viola and S. Lloyd, Dynamical suppression of decoherence in two-state quantum systems, Phys. Rev. A **58**, 2733 (1998).

[73] T. H. Taminiau, J. J. T. Wagenaar, T. van der Sar, F. Jelezko, V. V. Dobrovitski, and R. Hanson, Detection and Control of Individual Nuclear Spins Using a Weakly Coupled Electron Spin, Phys. Rev. Lett. **109**, 137602 (2012).

[74] S. Kolkowitz, Q. P. Unterreithmeier, S. D. Bennett, and M. D. Lukin, Sensing Distant Nuclear Spins with a Single Electron Spin, Phys. Rev. Lett. **109**, 137601 (2012).

[75] H. Y. Carr and E. M. Purcell, Effects of diffusion on free precession in nuclear magnetic resonance experiments, Phys. Rev. **94**, 630 (1954).

[76] T. Gullion, D. B. Baker, and M. S. Conradi, New, compensated Carr-Purcell sequences, J. Magn. Reson. **89**, 479 (1990).

[77] D. T. Gillespie, Exact numerical simulation of the Ornstein-Uhlenbeck process and its integral, Phys. Rev. E **54**, 2084 (1996).

[78] G. T. Genov, Y. Ben-Shalom, F. Jelezko, A. Retzker, and N. Bar-Gill, Efficient and robust signal sensing by sequences of adiabatic chirped pulses, Phys. Rev. Research **2**, 033216 (2020).

[79] R. Heck, O. Vuculescu, J. J. Sørensen, J. Zoller, M. G. Andreasen, M. G. Bason, P. Ejlertsen, O. Elíasson, P. Haikka,

J. S. Laustsen, L. L. Nielsen, A. Mao, R. Müller, M. Napolitano, M. K. Pedersen, A. R. Thorsen, C. Bergenholtz, T. Calarco, S. Montangero, and J. F. Sherson, Remote optimization of an ultracold atoms experiment by experts and citizen scientists, Proc. Natl. Acad. Sci. USA **115**, E11231 (2018).

[80] A. Omran, H. Levine, A. Keesling, G. Semeghini, T. T. Wang, S. Ebadi, H. Bernien, A. S. Zibrov, H. Pichler, S. Choi, J. Cui, M. Rossignolo, P. Rembold, S. Montangero, T. Calarco, M. Endres, M. Greiner, V. Vuletić, and M. D. Lukin, Generation and manipulation of Schrödinger cat states in Rydberg atom arrays, Science **365**, 570 (2019).

[81] Z. Wang, J. Casanova, and M. B. Plenio, Enhancing the robustness of dynamical decoupling sequences with correlated random phases, Symmetry **12**, 730 (2020).